Monthly Notices
of the
ROYAL ASTRONOMICAL SOCIETY

MNRAS **473,** 4297–4305 (2018)
Advance Access publication 2017 October 10

doi:10.1093/mnras/stx2635

A scale-dependent bias on linear scales: the case for H I intensity mapping at $z = 1$

Aurélie Pénin,[1]★ Obinna Umeh[2] and Mario G. Santos[2,3]

[1]*Astrophysics and Cosmology Research Unit, School of Mathematics Statistics and Computer Science, University of KwaZulu-Natal, Durban 4041, South Africa*
[2]*Department of Physics and Astrophysics, University of the Western Cape, Cape Town 7535, South Africa*
[3]*SKA South Africa, The Park, Cape Town 7405, South Africa*

Accepted 2017 October 6. Received 2017 October 5; in original form 2017 June 20

ABSTRACT

Neutral hydrogen (H I) will soon be the dark matter tracer observed over the largest volumes of Universe, thanks to the 21-cm intensity mapping technique. To unveil cosmological information, it is indispensable to understand the H I distribution with respect to dark matter. Using a full one-loop derivation of the power spectrum of H I, we show that higher order corrections change the amplitude and shape of the power spectrum on typical cosmological (linear) scales. These effects go beyond the expected dark matter non-linear corrections and include non-linearities in the way the H I signal traces dark matter. We show that, on linear scales at $z = 1$, the H I bias drops by up to 15 per cent in both real and redshift space, which results in underpredicting the mass of the haloes in which H I lies. Non-linear corrections give rise to a significant scale dependence when redshift space distortions arise, in particular on the scale range of the baryonic acoustic oscillations (BAOs). There is a factor of 5 difference between the linear and full H I power spectra over the whole BAO scale range, which modifies the ratios between the peaks. This effect will also be seen in other types of survey and it will be essential to take it into account in future experiments in order to match the expectations of precision cosmology.

Key words: large-scale structure of Universe – cosmology: theory.

1 INTRODUCTION

Future neutral hydrogen (H I) experiments such as the Square Kilometer Array (SKA, Santos et al. 2015), its pathfinder MeerKAT, the Canadian Hydrogen Intensity Mapping Experiment (CHIME, Newburgh et al. 2014), the Hydrogen Intensity and Real-time Analysis eXperiment (HIRAX, Newburgh et al. 2016) and the Baryon acoustic oscillations In Neutral Gas Observations (BINGO, Battye et al. 2013) will map the cosmological neutral hydrogen within unprecedented volumes of the Universe, thanks to the line intensity mapping (IM) technique. This technique relies on the measurement of the H I integrated intensity from hundreds of galaxies in one single large voxel (3D pixel) instead of detecting individual H I galaxies. The observed volumes will allow unrivalled constraints on cosmology (e.g. Bull et al. 2015). Nevertheless, to achieve the expected levels of accuracy, one needs to understand how H I relates to the underlying dark matter distribution. Current H I observations are quite sparse. At $z \sim 0$, H I is observed in emission at 21 cm but current detections weaken quickly and vanish at $z > 0.1$. At intermediate and higher redshifts, the main tracer of H I is Damped Ly α systems (DLAs), objects with $N_{\rm H\,I} > 10^{20.3}\,{\rm cm}^{-2}$ displaying a 21 cm line in absorption in the spectrum of a distant quasar. As they are optically thick, hydrogen into their midst is self-shielded and remains neutral. DLAs are actually thought to host most of the neutral gas within $0 < z < 5$ (Wolfe et al. 1986; Lanzetta, Wolfe & Turnshek 1995; Wolfe, Gawiser & Prochaska 2005) and hence to contain a significant reservoir of neutral gas for star formation at high redshift. Combining emission and absorption measurements, the redshift evolution of the fraction density of H I $\Omega_{\rm H\,I}$ has been shown to decrease slightly from high to low redshift (Crighton et al. 2015; Sánchez-Ramírez et al. 2016). Such a mild but somewhat steady evolution leads to the picture of a balance between consumption and replenishment of the gas reservoir. Notwithstanding, even though measurements are used altogether, 21 cm emission and 21 cm absorption line surveys might not target the same population of objects. This is crucial in order to clarify what is the H I bias. DLAs at high redshift might not belong to the same population than H I galaxies at low redshift. Properties of DLA hosts remain largely unknown, either because the background quasar is several magnitudes brighter or because they are too faint to be detected by current spectrographs ($m > 25$, Rauch

★ E-mail: aurelie.c.penin@gmail.com

et al. 2008; Cen 2012). When it comes to the mass of their host dark matter haloes, there seems to be a tension between 21 cm low redshift galaxies and DLAs. There are only a handful of measurements of H I and DLA biases. Martin et al. (2012) measured $b_{\rm H\,I} \sim 0.8$ at $z \sim 0$ in the ALFALFA survey, while Chang et al. (2010), Masui et al. (2013) and Switzer et al. (2013) measured the product $\Omega_{\rm H\,I} b_{\rm H\,I}$ in IM data taken with the Green Bank Telescope at $z \sim 0.8$. The latter used the IM data in auto-correlation, while the former cross-correlated them with galaxy surveys to circumvent the contamination of foregrounds residuals. Font-Ribera et al. (2012) measured $b_{\rm DLA} = 2.17 \pm 0.2$ at $z \sim 2.3$ in the Baryon Oscillation Spectroscopic Survey. Such a value leads to host dark matter haloes of $10^{11.5}\,{\rm M}_\odot$ as compared to the $10^{9-11}\,{\rm M}_\odot$ found with 21 cm measurements as well as in simulations (Pontzen et al. 2008; Rahmati & Schaye 2014). To reconcile bias measurements, Padmanabhan, Choudhury & Refregier (2016) argued that there must be a significant change in the properties of H I-bearing systems. The knowledge of the H I bias requires to understand how H I populates dark matter haloes. Even though it is widely accepted that H I is within galaxies at $z < 5$, today a simple relation between dark matter halo and H I masses (MHIMh) is used, with a certain gas profile when necessary (which is not for the bias). The MHIMh relation is measured in hydrodynamical simulations often assuming a simple power law (Davé et al. 2013; Kim et al. 2017; Villaescusa-Navarro et al. 2016), inspired from observations (Bagla, Khandai & Datta 2010) or parametrized and fitted on data (Barnes & Haehnelt 2010, 2014; Padmanabhan et al. 2016; Padmanabhan & Refregier 2017). Lately, Padmanabhan & Kulkarni (2017) derived the MHIMh relation using the abundance matching technique where the halo mass function is matched to the H I mass function. Even if these different schemes can strongly differ, they all lead to similar values of the linear H I bias. On non-linear scales, the H I bias has been barely investigated yet, while it contains a wealth of information on cosmology and, above all, on the MHIMh relation. To date, the scale dependence of the H I bias has been measured in two ways: in hydrodynamical simulations (Villaescusa-Navarro et al. 2014) and in *N*-body simulations where haloes are populated with H I through an empirical relation (Sarkar, Bharadwaj & Anathpindika 2016; Seehars et al. 2016). However, these methods suffer from a few limitations. In hydrodynamical simulations, the bias is sensitive to the physical processes that are included in the simulation, and, first and foremost, to the resolution. For instance, several zoom-in simulations will not lead to the same value of the bias at the same common scale. In addition, hydrodynamic simulations can hardly access linear scales and both approaches are computationally heavy. The investigation of the influence of the MHIMh scheme on the H I bias on the full scale range requires a more flexible approach. We use the full one-loop calculation of Umeh, Maartens & Santos (2016) and Umeh (2017) to compute the non-linear power spectrum of H I. It relies on high-order H I biases that are computed with the halo model for each MHIMh prescription. We compute the power spectrum and the bias of H I in both real and redshift space and show that non-linear terms have a significant contribution on linear scales. We limit our analysis to $z = 1$, which is one of the most targeted redshifts for baryonic acoustic oscillation (BAO) measurements. This paper is organized as follows. We begin with reviewing the theoretical framework of the H I power spectrum and listing the MHIMh relations we use in Section 2. Secondly, we compute the power spectrum and bias in real space with which we examine the mass of haloes in which H I lies in Section 3. Thirdly, we carry a similar analysis in redshift space and discuss its cosmological implications in Section 4. We conclude in Section 5

Throughout the article, we use the Planck 2014 Cosmology (Planck Collaboration XVI. 2014).

2 MODELLING THE H I POWER SPECTRUM

2.1 The power spectrum

The average H I brightness temperature is given by (Battye et al. 2013)

$$\overline{T}(z) = 566\,h \left(\frac{H_0}{H(z)}\right)\left(\frac{\Omega_{\rm H\,I}(z)}{0.003}\right)(1+z)^2 \ \mu{\rm K}, \tag{1}$$

where the H I density fraction is defined as $\Omega_{\rm H\,I} = \rho_{\rm H\,I}/\rho_{c,0}$ with $\rho_{c,0}$ is the critical density of the Universe today. The fluctuating part is

$$T(z, \boldsymbol{x}) = \overline{T}(z)\,(1 + \delta_{\rm H\,I}(\boldsymbol{x})) \tag{2}$$

with $\delta_{\rm H\,I}(\boldsymbol{x})$ the H I density fluctuation at position $\boldsymbol{x}$, hence, in Fourier space

$$\langle T(z, \boldsymbol{k}) T^\star(z, \boldsymbol{k}')\rangle = (2\pi)^3 P_{\rm H\,I}(k, z)\delta^3(\boldsymbol{k} - \boldsymbol{k}'). \tag{3}$$

Carrying a full one-loop derivation of the H I brightness temperature in Perturbation Theory (Bernardeau et al. 2002), the power spectrum of H I in real space at redshift z is

$$P_{\rm H\,I}(z, k) = P^{11}_{\rm H\,I}(z, k) + P^{22}_{\rm H\,I}(z, k) + P^{13}_{\rm H\,I}(z, k), \tag{4}$$

where $P^{11}_{\rm H\,I}(z, k)$ is the linear power spectrum (tree level), while $P^{22}_{\rm H\,I}(z, k)$ and $P^{13}_{\rm H\,I}(z, k)$ are the non-linear corrections. For clarity purposes, we will not specify the redshift dependence in the following. Following Umeh et al. (2016) and Umeh (2017), the three terms of $P_{\rm H\,I}(k)$ are

$$P^{11}_{\rm H\,I}(k) = \overline{T}^2\, b_1^2\, P^{11}_{\rm m}(k), \tag{5}$$

$$P^{22}_{\rm H\,I}(k) = \frac{\overline{T}^2}{2}\int \frac{{\rm d}^3 k_1}{(2\pi)^3}[b_1\, F_2(\boldsymbol{k}_1, \boldsymbol{k}_2) + b_2]^2 \times P^{11}_{\rm m}(k_2)\, P^{11}_{\rm m}(k_1), \tag{6}$$

$$P^{13}_{\rm H\,I}(k) = \overline{T}^2\, b_1 \left\{\left(b_3 + \frac{68}{21}b_2\right)\sigma_\Lambda^2 P^{11}_{\rm m}(k) + b_1\, P^{13}_{\rm m}(k)\right\}, \tag{7}$$

where $k_2 = |\boldsymbol{k}_1 - \boldsymbol{k}|$. b_1, b_2 and b_3 are the linear, second and third-order H I biases, respectively. The latter are the higher terms of the bias expanded in Taylor series, which means assuming that the H I bias is local. F_2 is the non-linear density kernel defined in Appendix A. Finally, σ_Λ, the variance of the dark matter field, is

$$\sigma_\Lambda^2 = \int_{k_{\rm min}}^{k_{\rm max}} \frac{{\rm d}^3 k}{(2\pi)^3} P_{\rm m}(k). \tag{8}$$

For simplicity, we set $k_{\rm max}$ to the non-linear dispersion scale, $k_{\rm NL} = 0.2\,h(1+z)^{2/(2+n_{\rm s})}\,{\rm Mpc}^{-1}$ with $n_{\rm s}$ the spectral index. In redshift space, the 3D power spectrum of H I on linear and quasi-linear scales at scale k, and μ, the cosine of the angle between the line of sight and the separation vector $\boldsymbol{k}$, writes

$$P_{\rm H\,I}(k, \mu) = P^{11}_{\rm H\,I}(k, \mu) + P^{22}_{\rm H\,I}(k, \mu) + P^{13}_{\rm H\,I}(k, \mu). \tag{9}$$

Following Kaiser (1987), the linear term in redshift space is

$$P^{11}_{\rm H\,I}(k, \mu) = \overline{T}^2\left[b_1 + f\,\mu^2\right]^2\, P^{11}_{\rm m}(k) \tag{10}$$

with $\mu = k_\parallel/k$, $P_{\rm m}(k)$ the linear power spectrum of matter, and f the linear growth rate. We compute the former using the transfer function of Eisenstein & Hu (1998) and assume $f(z) = \Omega_{\rm m}(z)^\gamma$ with

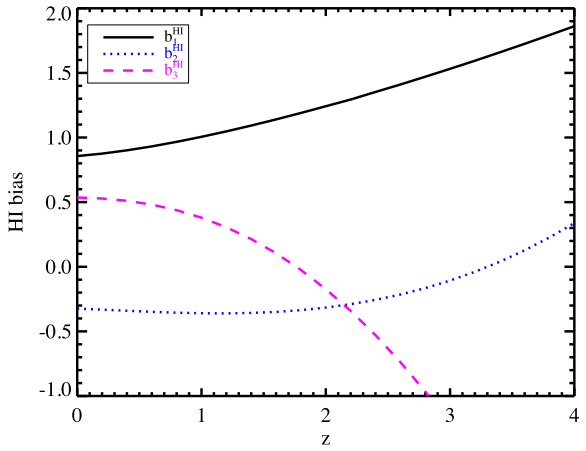

Figure 1. H I biases computed with equation (14) using the HOD A prescription for the relation between H I and halo mass at $z = 1$.

$\gamma = 0.55$ for ΛCDM (Peebles 1980; Linder 2005). Following Umeh et al. (2016) and Umeh (2017), the one-loop corrections are

$$P^{22}_{\rm H\,I}(k,\mu) = \frac{\overline{T}^2}{2}\int \frac{{\rm d}^3k_1}{(2\pi)^3}\left[b_1\,F_2(\boldsymbol{k}_1,\boldsymbol{k}_2) + \mu^2 G_2(\boldsymbol{k}_1,\boldsymbol{k}_2) + b_2 + K_R(\boldsymbol{k}_1,\boldsymbol{k}_2)\right]^2 \times P^{11}_{\rm m}(k_2)\,P^{11}_{\rm m}(k_1), \quad (11)$$

$$P^{13}_{\rm H\,I}(k,\mu) = \overline{T}^2\left(b_1+\mu^2 f\right) \times\left\{\left[\left(b_3+\frac{68}{21}b_2\right)\sigma^2_\Lambda + I_R(k,\mu)\right]P^{11}_{\rm m}(k) + \left[b_1\,P^{13}_{\rm m}(k) + \mu^2\,f\,P^{13}_\theta(k)\right]\right\}, \quad (12)$$

where $P^{13}_{\rm m}(k)$ and $P^{13}_\theta(k)$ are the third-order matter power spectrum and velocity field power spectrum, respectively. Their expressions along with that of $I_R(k,\mu)$ are listed in Appendix A. Finally, several kernels are involved in the computation of the $P^{22}_{\rm H\,I}(k,\mu)$ term: G_2 induced by peculiar velocities at second order and K_R arises from non-linear mode coupling (velocity–velocity and velocity–density, Bernardeau et al. 2002). Their expressions are also given in Appendix A.

2.2 H I quantities

H I -related quantities such as densities and biases are computed using the halo model that provides a description of the clustering of dark matter haloes at both linear and non-linear scales (Cooray & Sheth 2002). It relies on the halo mass function ${\rm d}n/{\rm d}M$ and the associated nth order halo biases $b^{\rm h}_n(M)$ measured in N-body simulations. We use the prescriptions of Sheth & Tormen (1999). The comoving density of H I writes

$$\rho_{\rm H\,I} = \int {\rm d}M \frac{{\rm d}n}{{\rm d}M} M_{\rm H\,I}(M). \quad (13)$$

The nth order H I biases are

$$b^{\rm H\,I}_n = \frac{1}{\rho_{\rm H\,I}}\int {\rm d}M \frac{{\rm d}n}{{\rm d}M} b^{\rm h}_n(M)\,M_{\rm H\,I}(M), \quad (14)$$

where $M_{\rm H\,I}(M)$ is the relation between the H I mass and the halo mass (see Section 2.3). Fig. 1 shows an example of a set of biases. Note that only the first-order bias is always positive, while the two others change sign. All of them increase for high halo masses. We will use the terms *linear* and *first -order* bias interchangeably.

2.3 The H I mass–halo mass relation

The distribution of H I within the large scale structure is rather unclear today. It is believed that in the post-reionization era most of H I lies within galaxies while only a negligible fraction is diffuse (Seehars et al. 2016). It is often simply parametrized by relating the mass of H I to the mass of its host dark matter halo through a simple power law including, or not, a cut-off at small and high halo masses. We compile here several MHIMh relations that have been used or estimated using both hydrodynamical simulations and parametrized models fitted on data measurements. We also consider a DLA model.

(i) Bagla10: One relation that has been widely used is that of Bagla et al. (2010). It has been inspired from quasar observations and assumes that there is no H I in high mass haloes:

$$M_{\rm H\,I}(M) = \frac{f_3\,M}{1+\frac{M}{M_{\rm max}}} \quad \text{for } M \geq M_{\rm min}, \quad (15)$$

where f_3 comes from the normalization to $\Omega_{\rm H\,I}$. This prescription is commonly used for studies of 21 cm IM (amongst others, Villaescusa-Navarro et al. 2014; Sarkar et al. 2016; Seehars et al. 2016). $M_{\rm min}$ and $M_{\rm max}$ are the limits for a dark matter halo to host H I. They assume that only haloes with $30 < v_{\rm circ} < 200\,{\rm km\,s^{-1}}$ host H I, which translates into lower and upper bounds, $M_{\rm min}$ and $M_{\rm max}$ through

$$v_{\rm circ} = 30\sqrt{1+z}\left(\frac{M}{10^{10}\,{\rm M}_\odot}\right)^{1/3}\ {\rm km\,s^{-1}} \quad (16)$$

(ii) AGN: Nevertheless, Villaescusa-Navarro et al. (2016) measured the MHIMh relation in hydrodynamical simulations, including AGN feedback, and showed that there is H I in haloes that have $v_{\rm circ} > 200\,{\rm km\,s^{-1}}$. They measured $M_{\rm H\,I}(M) = {\rm e}^\alpha M^\gamma$ and fitted α and γ up to redshift 2.

(iii) DLA50: A prescription adapted from DLA studies (Barnes & Haehnelt 2010, 2014) by Padmanabhan et al. (2016):

$$M_{\rm H\,I}(M) = \alpha\,f_{\rm H,c}\,M\,\exp\left[-\left(\frac{v_{\rm c,0}}{v_{\rm c}(M)}\right)^3\right]\exp\left[-\left(\frac{v_{\rm c,1}}{v_{\rm c}(M)}\right)^3\right], \quad (17)$$

where α is the ratio of H I within haloes and cosmic H I, $f_{\rm H,c} = (1-Y_p)\Omega_{\rm b}/\Omega_{\rm m}$ is the cosmic hydrogen fraction with Y_p the cosmological helium fraction by mass and $v_{\rm c}(M)$ is the virial velocity of a halo (Bullock et al. 2001):

$$v_{\rm c}(M) = 96.6\ {\rm km\,s^{-1}}\left(\frac{\Delta_v\Omega_{\rm m}h^2}{24.4}\right)^{1/6}\left(\frac{1+z}{3.3}\right)^{1/2}\left(\frac{M}{10^{11}\,{\rm M}_\odot}\right)^{1/3} \quad (18)$$

with Δ_v the mean overdensity of the halo that we take to be 200. For DLAs, Padmanabhan et al. (2016) considered $v_{\rm c,\,0} = 50\,{\rm km\,s^{-1}}$ and an infinite $v_{\rm c,\,1}$. They fitted α to measurements between redshift 0 and 4 (column density distributions, biases, $\Omega_{\rm H\,I}$ and the incidence rate).

(iv) 21 cm: Padmanabhan et al. (2016) adapted equation (17) to 21 cm IM observations using ad hoc velocity cuts $v_{\rm c,\,0} = 30\,{\rm km\,s^{-1}}$ and $v_{\rm c,\,1} = 200\,{\rm km\,s^{-1}}$. Similarly to the DLA50 model, Padmanabhan et al. (2016) fitted α on the same measurements.

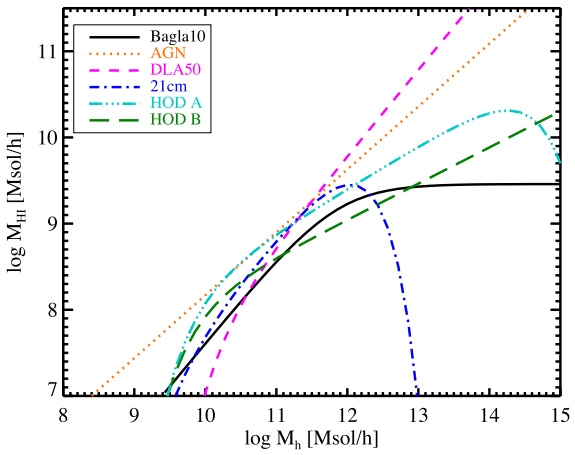

Figure 2. Relations between the H I mass and the halo mass at $z = 1$.

Note that in both the latter cases, the slope is fixed and equal to unity, which is higher than that measured in hydrosimulations.

(v) HOD A: Padmanabhan & Refregier (2017) improved equation (17) by introducing a flexible slope, β, as well as the velocity cut-offs:

$$M_{\rm H\,I}(M) = \alpha\, f_{\rm H,c}\, M \left(\frac{M}{10^{11} h^{-1}\,{\rm M}_\odot}\right)^{\beta} \exp\left[-\left(\frac{v_{\rm c,0}}{v_{\rm c}(M)}\right)^3\right] \times \exp\left[-\left(\frac{v_{\rm c,1}}{v_{\rm c}(M)}\right)^3\right], \quad (19)$$

where α, β, $v_{\rm c,\,0}$ and $v_{\rm c,\,1}$ are free parameters and fitted on data measurements.

(vi) HOD B: Lastly, Padmanabhan, Refregier & Amara (2017) fitted an updated version of equation (19)

$$M_{\rm H\,I}(M) = \alpha\, f_{\rm H,c}\, M \left(\frac{M}{10^{11} h^{-1}\,{\rm M}_\odot}\right)^{\beta} \exp\left[-\left(\frac{v_{\rm c,0}}{v_{\rm c}(M)}\right)^3\right] \quad (20)$$

on all the available measurements including galaxy clustering. Their free parameters are β and α.

All these prescriptions are shown in Fig. 2 at $z = 1$. They vary in shape, amplitude and slope. Clearly, the DLA50 scheme favours high halo masses as compared to the other models. We limit our analysis to $z = 1$, the values of the free parameters are given in Table 1.

3 THE H I POWER SPECTRUM IN REAL SPACE

In this section, we compute the non-linear H I power spectrum in real space using all the above MHIMh models. We first describe the non-linear contributions to the power spectrum and show that the bias is neither constant nor linear on so-called linear scales. We discuss the implications of that effective bias on our understanding of the distribution of H I and compare this modelling approach to others.

3.1 A non-linear bias on linear scales

The total H I power spectrum along with the non-linear contributions are shown in Fig. 3 for model HOD A. Contrary to our expectations, both $P^{22}_{\rm H\,I}$ and $P^{13}_{\rm H\,I}$ terms have significant contributions on linear scales. These contributions arise from the coupling of short and long wavelength modes. The $P^{13}_{\rm H\,I}$ term is negative and proportional to the matter power spectrum. Therefore, on linear scales, it lowers the amplitude of the H I power spectrum by ∼25 per cent as compared to a standard biased power spectrum. Hence, the actual H I bias is lower than the linear H I bias. The $P^{22}_{\rm H\,I}$ term is constant on linear scales, which induces a scale dependence of the H I bias on the largest scales. The flat contribution to the $P^{22}_{\rm H\,I}$ term (the dot–dashed line) is simply proportional to $b_2^{\rm H\,I}$ while, on those scales, the $P^{13}_{\rm H\,I}$ term is a function of $b_1^{\rm H\,I}$, $b_2^{\rm H\,I}$ and $b_3^{\rm H\,I}$. The latter depend on the MHIMh prescriptions and are listed in Table 1. While the $b_1^{\rm H\,I}$s vary by ∼13 per cent amongst the different prescriptions, the variation strongly increases at higher orders. Indeed $b_2^{\rm H\,I}$s and $b_3^{\rm H\,I}$s differ by 35 per cent and 74 per cent, respectively. Hence, the shape of the H I bias depends on the MHIMh prescription as shown in Fig. 4. Hereafter, we will call H I *effective* bias the following :

$$b^{\rm eff}_{\rm H\,I}(k) = \frac{1}{\overline{T}_{\rm H\,I}} \sqrt{\frac{P_{\rm H\,I}(k)}{P^{11}_{\rm m}(k)}}. \quad (21)$$

The right-hand panel of Fig. 4 shows the ratio $1/\overline{T}_{\rm H\,I}\sqrt{P_{\rm H\,I}(k)/P^{\rm NL}_{\rm m}(k)}$, where $P^{\rm NL}_{\rm m}(k)$ is the non-linear matter power spectrum computed using the same perturbation theory framework (see Appendix A). The normalization by the mean H I temperature is to focus only on the bias and avoid additional amplitude variations. Indeed, the H I temperature is a function of $\Omega_{\rm H\,I}$, therefore of the MHIMh relation (see equation (1) and Table 1). On the largest scales, there is only a few percent difference between the different prescriptions. We will not discuss them here as General Relativity corrections must be taken into account on ultra-large scales. On non-linear scales, regardless of the MHIMh relation, we recover a bias well below 1, meaning that H I galaxies are highly antibiased while they are only slightly on linear scales (Marín et al. 2010; Martin et al. 2012). At $k > 0.2\,h\,{\rm Mpc}^{-1}$, our biases are of the same order of magnitude than that of Sarkar et al. (2016) as shown in the right-hand panel of Fig. 4. Their dip is deeper because their bias on linear scales is higher than ours. Nevertheless, they are consistent as explained in the following and in Section 3.3. On linear scales, there is, at most, a difference of 10 per cent in the amplitude of the models and 15 per cent at $k = 1\,h\,{\rm Mpc}^{-1}$. Regardless of the MHIMh prescription, the *effective* bias, $b^{\rm eff}_{\rm H\,I}$, is

Table 1. Free parameters of the MHIMh prescriptions along with the associated H I biases and mean temperatures at $z = 1$.

Model	Parameters	b_1	b_2	b_3	$b_{\rm eff}$	$T_{\rm H\,I} \times 10^4$ K
Bagla10	None	0.93	−0.41	0.62	0.80	1.65
AGN	$\alpha = 0.73$, $\gamma = 2$	0.91	−0.27	0.41	0.82	12.14
21 cm	$\alpha = 0.15$	0.96	−0.42	0.60	0.81	2.43
HOD A	$\log v_{\rm c,\,0} = 1.58$, $\log v_{\rm c,\,1} = 3.14$, $\alpha = 0.17$, $\beta = -0.5$	1.00	−0.35	0.38	0.82	4.38
HOD B	$\log_{10} v_{\rm c,\,0} = 1.56$, $\alpha = 0.09$, $\beta = -0.58$	0.96	−0.37	0.49	0.85	2.55
DLA50	$\alpha = 0.13$	1.64	0.56	−1.27	1.74	49.94

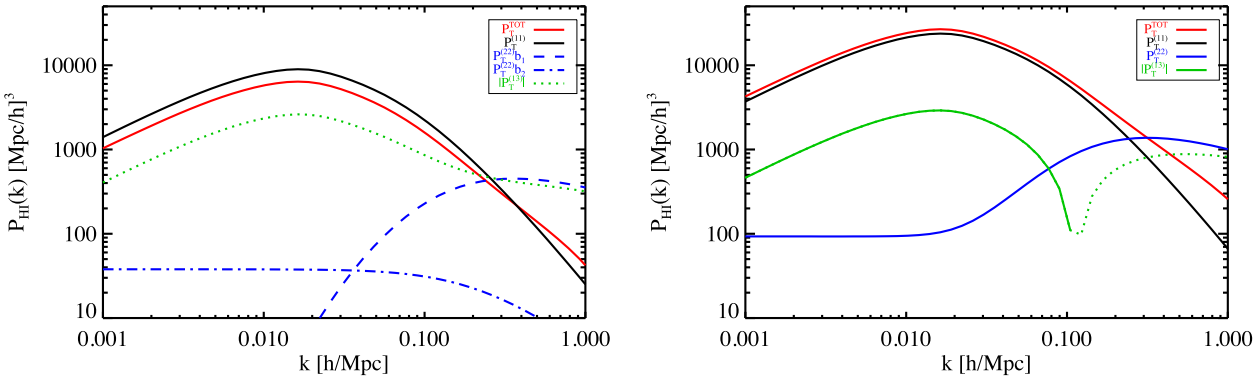

Figure 3. Linear and non-linear contributions to the real space H I power spectra for the HOD A prescription (left-hand panel) and the DLA50 one (right-hand panel). Note that green lines show the absolute value of the P_{13} term and the dotted line is the negative part. The dashed and dot–dashed blue lines are the b_1 and b_2 components of the P_{22} term, respectively.

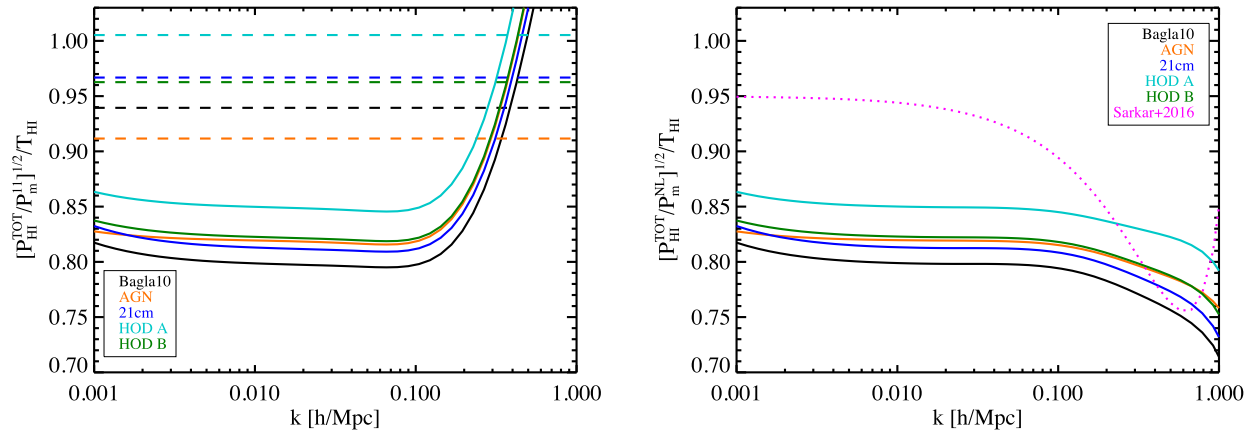

Figure 4. Scale dependence of the H I bias (left-hand panel) and the ratio $\sqrt{P_{\rm HI}(k)/P_{\rm m}^{\rm NL}(k)}/\overline{T}_{\rm HI}$ (right-hand panel) for the different MHIMh prescriptions in real space. Horizontal dashed lines are the linear biases for each MHIMh models computed with equation (14). The magenta dotted line is the H I bias of Sarkar et al. (2016). The $P_{\rm m}^{11}$ and $P_{\rm m}^{\rm NL}$ are the linear and non-linear power spectra of matter, respectively.

lower than the linear one. Their values at $k = 0.01\,h\,{\rm Mpc}^{-1}$ are listed in Table 1 along with the associated linear biases. On linear scales, effective biases are always lower by 10–15 per cent than their linear counterpart. They can be approximated, in real space, by

$$b_1^{\rm H\,I} \rightarrow b_{\rm H\,I}^{\rm eff} \approx b_1^{\rm H\,I} + \frac{1}{2}\left(b_3^{\rm H\,I} + \frac{68}{21}b_2^{\rm H\,I}\right)\sigma_\Lambda^2. \quad (22)$$

It has consequences on our understanding of H I within the large-scale structure. The assumption that the measured H I bias on large scales is linear leads to an underestimation of that linear bias and therefore of the halo mass hosting H I. Hence, H I lies in slightly more massive haloes than thought.

3.2 In which haloes does H I lie?

Currently, there is a tension between halo masses of H I-bearing systems, in particular between observations of H I galaxies at low redshift and those of DLAs at higher redshift as highlighted by Padmanabhan et al. (2016). They fitted all H I available measurements (DLA incidence rates, column densities, biases, H I fractional densities and biases) at several redshifts with both DLA- and 21 cm-based models (our schemes DLA50 and 21cm, amongst others). They showed that the 21 cm based model fitting all measurements systematically underpredicts the DLA bias. Similarly, DLA models, which are tuned to reproduce the DLA bias, always overpredict $\Omega_{\rm H\,I}b_{\rm H\,I}$. Their two DLA models have low velocity cut-offs of 50 and 90 km s^{-1}, which implies that there is no or only a low amount of neutral hydrogen in low mass haloes. While Barnes & Haehnelt (2014) suggested that it could be caused by a strong stellar feedback, it remains inconsistent with H I observations at low redshift. In addition, the discrepancy holds when varying the H I concentration. It is important to note that the discrepancy is only at the level of the biases, hence, the tension is between the host haloes of low and high redshift H I-bearing systems. Padmanabhan et al. (2016) argued that there must be a dramatic change in the properties of these systems over $0 < z < 3$ to have these halo masses on the same evolution path. This idea is strengthened by Padmanabhan & Refregier (2017), who introduced a halo occupation model inspired by both DLA and 21-cm emission framework (our HOD A model), using the same data set as the former together with the H I mass function at $z \sim 0$. Again, most of the observables are relatively well fitted but the DLA bias is, again, underpredicted while the high mass part of the H I mass function is overpredicted. Lately, Padmanabhan et al. (2017) carried a similar analysis with an updated version of the MHIMh relation (our HOD B model) adding the two-point correlation function (2PCF) of H I galaxies at small scales. By levering some degrees of freedom in the H I concentration, they did improve the overall quality of the fit but with an overpredicted 2PCF on large scales, a high mass tail

of the H I mass function and a too low DLA bias. It is clear that both models predict too many objects in high mass haloes and a H I bias that is too high. Indeed, fits are driven towards high halo masses by the DLA bias measurement, which might be flawed as it is inconsistent with most observations and simulations. The latter statement seems inconsistent with our previous argument, which is that H I lies in more massive haloes than we think. The non-linear corrections to the bias are of the order of 15 per cent at most, while the discrepancies between the predicted and measured H I biases are, at least, of 50 per cent. Therefore, the systematic error due to the assumption of a linear bias on large scales is concealed by the error induced by the DLA bias. We also consider a MHIMh relation adapted to DLAs, the DLA50 model. It is obvious from Fig. 2 that it favours higher mass haloes as compared to any other prescription. This translates into a higher linear bias and into a change of sign of $b_2^{\rm H\,I}$ and $b_3^{\rm H\,I}$ (see Table 1). $P_{\rm H\,I}^{13}$ becomes positive on large scales as shown in Fig. 3, which adds power to the H I power spectrum. Hence, the effective bias is higher than its linear counterpart in the case of DLAs. The amplitude of the power spectrum rises by 13 per cent, which translates into 7 per cent on the effective bias for the DLA50 model. Of course, the additional power increases when going towards even higher mass haloes. For instance, using a $v_{\rm c,\,0} = 90\,{\rm km\,s^{-1}}$ instead of $v_{\rm c,0} = 50\,{\rm km\,s^{-1}}$, which translates into minimum halo masses of $10^{10.04}$ and $10^{10.80}\,h^{-1}\,{\rm M}_\odot$ at $z = 1$, leads to an increase in power of 24 per cent and 11 per cent at the power spectrum and bias levels, respectively. Thus, DLA models overpredict the H I bias even more than previously thought, which enhances the tension between DLAs and 21-cm biases, preventing any reconciliation.

3.3 Consistency with other modelling approaches and clustering analysis

It is the coupling between small- and large-scale modes that gives rise to an effective bias different from the linear one. Therefore, the mismatch exists for any tracer of dark matter. Hence, one can wonder why it is not predicted by any other modelling approaches and why it has never been noticed in any clustering analysis. The answer to the first question is straightforward: models are constructed to predict a linear bias on linear scales. The procedure for modelling the clustering of any tracer is a distribution of haloes coming either from the halo model or from dark matter simulations that are filled in with the tracer. Therefore, only non-linearities coming from the evolution of the distribution of dark matter are present and not the ones coming from the distribution of the tracer, which is not the case in our approach. Indeed, it is the distribution of the tracer, the H I brightness temperature precisely, that has been perturbed. Therefore, our biases in Fig. 4 are consistent with that of Sarkar et al. (2016). They used a dark matter simulation in which they defined haloes that are assigned an H I mass through the Bagla10 model. On the largest scales, they measure a H I bias of 0.92 fully consistent with the linear bias of 0.94 computed through equation (14). Lastly, why a mismatch has not been noticed in clustering analysis yet as linearities are missing in current models? On linear scales, it is an offset of 15 per cent on the bias for H I at most and the scale dependency is only of a few per cent so it can be well concealed in the error bars. For instance, when fitting the parameters of a halo occupation distribution on a CF on both linear and non-linear scales, the halo mass thresholds hosting a central galaxy and one satellite galaxy would be found to be lower than it is in reality. Notwithstanding, this systematic error is lower than the statistical error on the fitted parameters in current clustering analysis. It will not be the case with stage IV experiments such as *Euclid* and SKA. In addition, in the era of precision cosmology, ignoring these corrections will lead to flawed estimations of cosmological parameters.

4 THE H I POWER SPECTRUM IN REDSHIFT SPACE

In this section, we extend the previous analysis to the anisotropic power spectrum of H I in redshift space. We first adopt a theoretical point of view, investigating the power spectrum as a function of k and μ to understand the effects of RSDs, and second, we compare the expected linear power spectrum to the full one in the transverse and radial directions.

4.1 The H I effective bias on linear scales

We begin by investigating the different contributions to the H I power spectrum in the two extreme directions: in the transverse one where $\mu = 0$, meaning that RSDs are null, and in the radial direction where $\mu = 1$ and, hence, RSDs are maximal. Fig. 5 shows the different terms contributing to the H I power spectrum for the prescription HOD A. We recover similar behaviours to those in real space. The $P_{\rm H\,I}^{22}$ term is constant on large scales ($k < 0.02\,h\,{\rm Mpc^{-1}}$) and rises towards small scales. The amplitude of the rise increases with μ as RSDs come in, they are contained in the G_2 and K_R terms as shown in the lower panel. Therefore, on small scales ($k > 0.2\,h\,{\rm Mpc^{-1}}$), non-linear contributions are maximal for $\mu = 1$ where fingers of God are recovered. Again, the $P_{\rm H\,I}^{13}$ term is negative and thus removes power to the H I power spectrum on linear scales. The amplitude of the removal decreases with μ: at the power spectrum level, it lowers from ∼25 per cent at $\mu = 0$ to ∼13 per cent at $\mu = 1$, respectively. The former is similar to the real space case. The effective bias in redshift space is

$$b_1^{\rm H\,I} \rightarrow b_{\rm H\,I}^{\rm eff}(k,\mu) \approx b_1^{\rm H\,I} + \frac{1}{2}\left[\left(b_3^{\rm H\,I} + \frac{68}{21}b_2^{\rm H\,I}\right)\sigma_\Lambda^2 + I_R(k,\mu)\right]. \tag{23}$$

The expression of I_R is given in Appendix A, and it is worth noticing that the effective bias is also a function of the growth factor. We will explore this in more details in future work. For $\mu \neq 0$, the effective bias cannot be computed directly because of RSD effects so we compare the full H I power spectrum to the linear Kaiser prediction $P_{\rm H\,I}^{11}(k,\mu) = \overline{T}^2[b_1 + f\,\mu^2]^2\,P_{\rm m}^{11}(k)$ in Fig. 6 for all MHIMh models. Regardless of the scale, they lead to ratios that are within 10 per cent and those differences lower with μ. On linear scales, the effective bias gets closer to the linear one as μ increases. We can also notice in the lower panel that RSD effects impact the power spectrum only at $\mu > 0.2$. On smaller scales, the rise is due to non-linear effects, only, at $\mu = 0$ and also to RSDs for $\mu > 0$. The slope of the rise scales with μ and it is exactly over the BAO scale range.

4.2 A scale-dependent H I bias on BAO scales

We will carry on the analysis using only the model HOD A. The bottom panel of Fig. 6 shows a scale dependence of the H I bias that is enhanced by RSD effects over the BAO scale range: the bias rises from 10 per cent at $\mu = 0$ to a factor 2 at $\mu = 1$. To adopt an observational point of view, we change the coordinates to transverse and radial directions in Fig. 7. The two top panels show the linear and total H I power spectra. At first glance, non-linear terms shift the turnover of the power spectrum towards higher

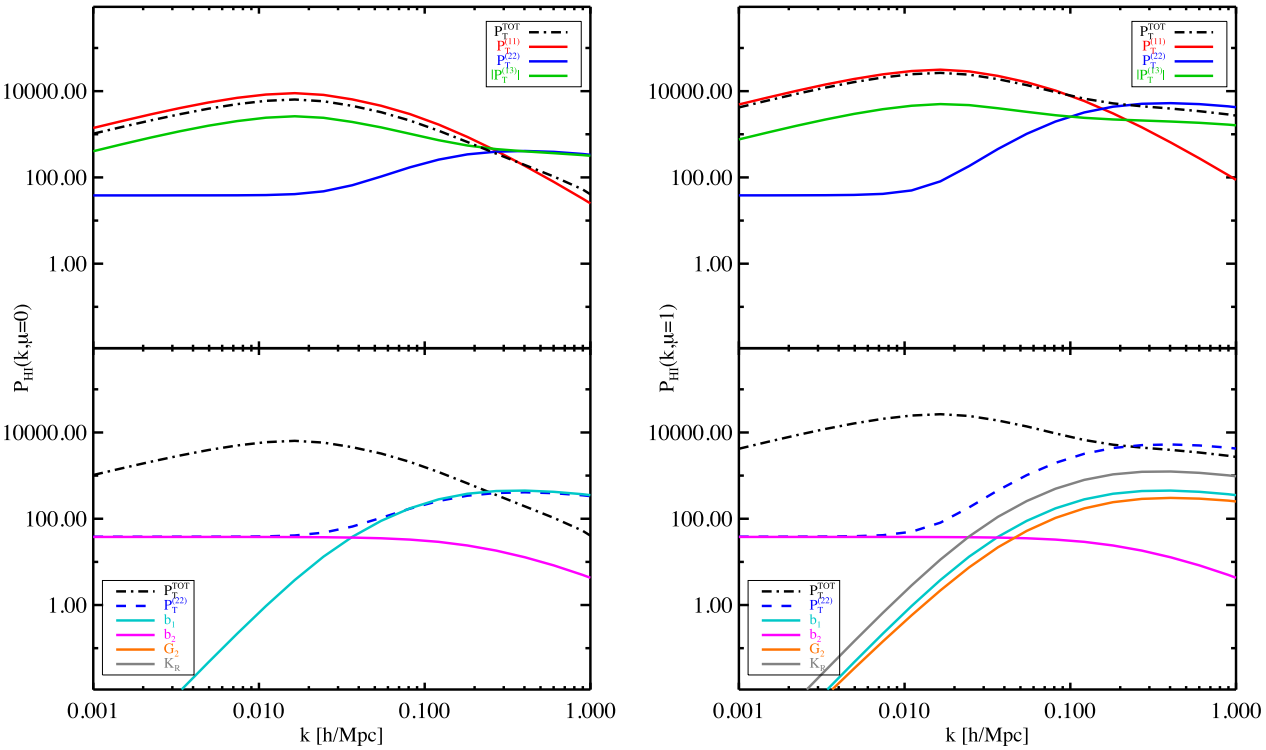

Figure 5. Anisotropic power spectrum in the transverse (left-hand panels) and radial (right-hand panels) directions for the MHIMh model HOD A. Top panels show the different non-linear terms while bottom panels show the detailed contributions to the $P_{\rm HI}^{22}$ term.

$k_\perp$ ($>0.1\,h\,{\rm Mpc}^{-1}$). They slightly enhance the signal along the $k_\perp$ direction while it is boosted along $k_\parallel$ by RSD effects. The lower panel of Fig. 7 shows the ratio between the linear and total H I power spectra. On large scales, $k_\parallel, k_\perp < 0.01\,h\,{\rm Mpc}^{-1}$, we recover a maximum ratio of 25 per cent. At small $k_\parallel$ and towards large $k_\perp$, non-linearities increase the amplitude of the H I power spectrum by a factor of 2, while at large $k_\parallel$, RSD effects dominate non-linear ones and make any $k_\perp$ dependence vanish. Over the BAO scale range, the H I power spectrum increases by a factor of 5 and 2 in the radial and transverse directions, respectively. Therefore, both non-linearities and RSD effects modify the ratios between the BAO peaks. It is therefore necessary to take non-linearities into account when estimating cosmological parameters. To circumvent the contamination by non-linear effects, one would preferentially measure the BAO peaks in the transverse direction, but Villaescusa-Navarro, Alonso & Viel (2017) showed that, in single dish mode, beyond a certain size, the beam of the instrument smears the wiggles out in the transverse direction and that BAOs can only be detected in the radial direction. This is a limitation for the SKA and Meerkat but not for BINGO, CHIME or HIRAX as they will have a higher angular resolution.

5 CONCLUSION

Radio telescopes are about to open a new window of observation on the Universe, in particular, using 21 cm IM. We investigate the non-linear power spectrum of H I in both real and redshift space and in the light of the relation between the halo mass and the H I mass. Our main result is that on linear scales, the H I bias is *not* constant but scale dependent. Using a full one-loop development in perturbation theory of the power spectrum of H I, we show that non-linear contributions remove power to the H I power spectrum on linear scales in both real and redshift space at $z = 1$. This result is contrary to our expectations and is not found in other modelling approaches. Commonly, a distribution of dark matter haloes is 'painted' with a baryonic tracer, so that only non-linearities coming from the distribution of dark matter are taken into account and not the ones coming from the evolution of the distribution of the tracer. In real space, the effective bias of H I is 10–15 per cent lower than the linear one, depending on the MHIMh relation. The assumption that the observed H I bias is linear underpredicts the actual linear bias, and hence, the mass of haloes hosting H I. In redshift space, the effective bias is also lower than its linear counterpart up to 15 per cent, and its scale dependence is highly sensitive to RSD effects. Over the BAO scale range, the H I bias rises with a slope that steepens with μ. Regardless of the MHIMh prescription, the difference between the linear and the full H I power spectra reaches a factor of 5, which can lead to a modification of the ratios between BAO peaks. Therefore, it will be crucial to take non-linearities into account when estimating cosmological parameters. The different MHIMh relations lead to variations of 15 per cent at most on the H I bias. It is within the error bars on any of the current H I bias measurements so it is not an issue at the moment. Nevertheless, it will be indispensable for the upcoming H I surveys. It is worth noting that the observable is the product $T_{\rm H\,I}\,b_{\rm H\,I}$, where the H I temperature is also a function of the MHIMh relation through $\Omega_{\rm H\,I}$. This product differs up to a factor of 7 between the different prescriptions. Thorough forecasts of the effect of non-linearities on the estimation of BAO peaks and in a broader way, cosmological parameters, are required, including the redshift evolution as H I is positively biased at higher redshift, therefore non-linearities add power to the power spectrum of H I. Lastly, this effect is not only present in H I IM surveys but in any galaxy surveys.

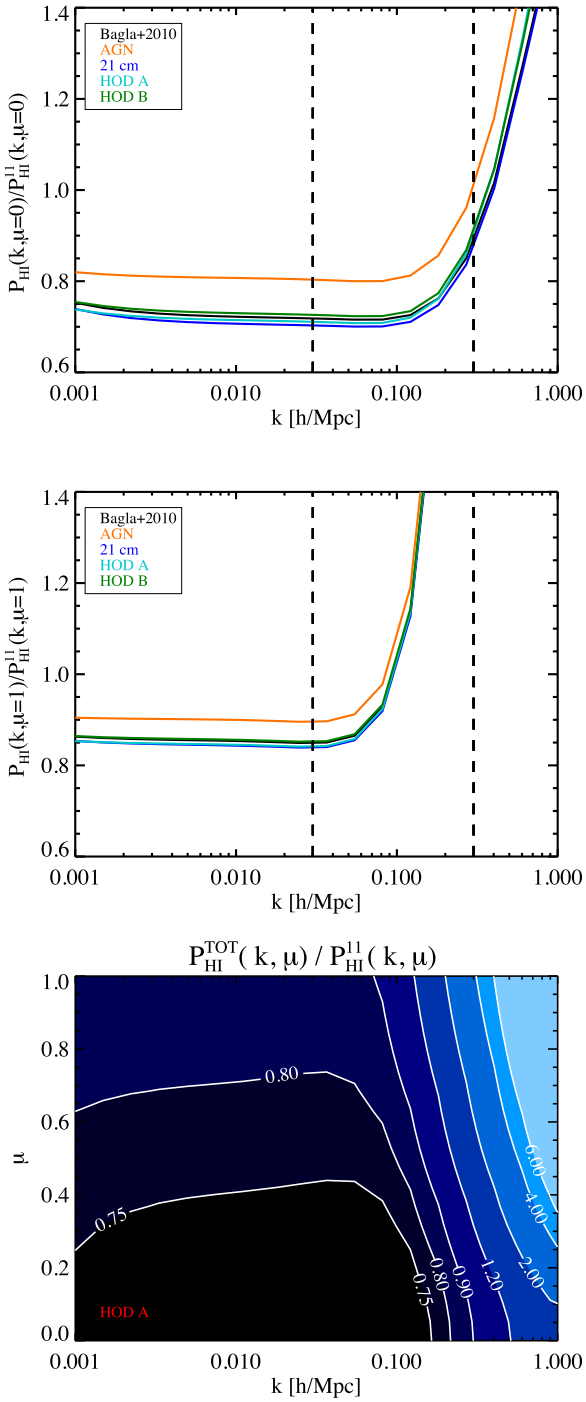

Figure 6. Ratios of the total H I power spectrum with the linear H I power spectrum for all the MHIMh prescriptions in the transverse (top panel) and the radial (middle panel) directions at $z = 1$. The lower panel shows the same ratio as a function of both μ and k for HOD A model. Black dashed lines are the BAO scale limits.

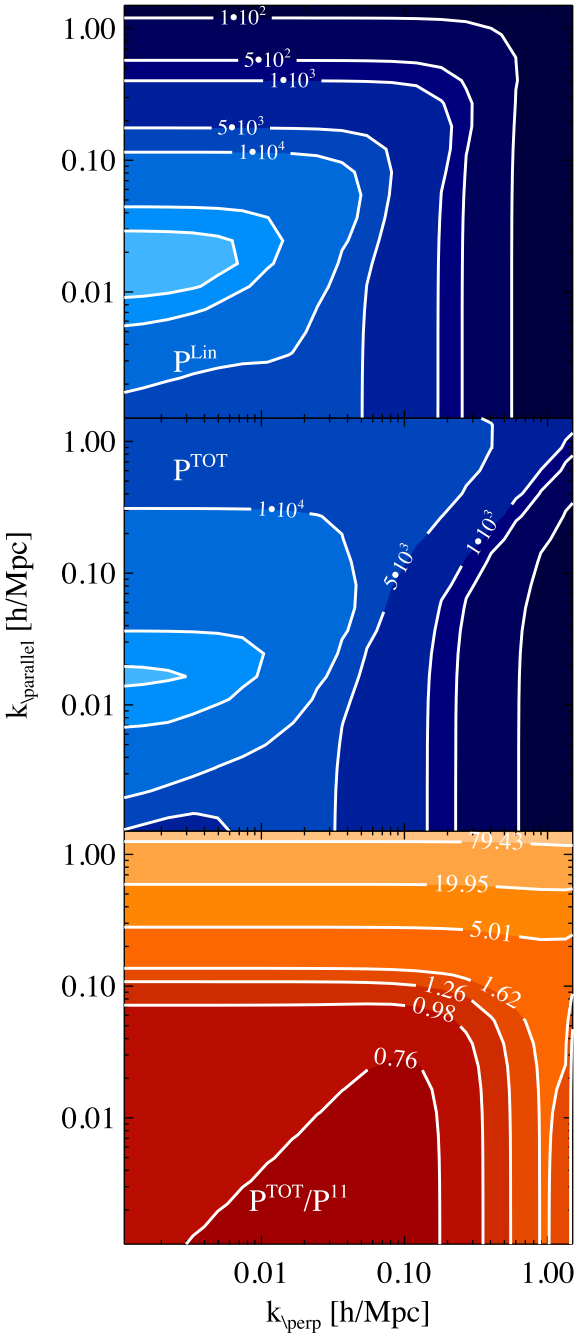

Figure 7. The anisotropic H I power spectrum for the HOD A model at $z = 1$ broken down into transverse and radial directions [in $(\mathrm{Mpc}\,h^{-1})^3$]. The top and middle panels display the linear and total power spectra, respectively, while the bottom panel shows the ratio between both power spectra.

ACKNOWLEDGEMENTS

The authors would like to thank Roy Marteens, Chris Clarkson, Jose Fonseca and Vincent Desjacques for useful discussions. They also would like to thank Debanjan Sarkar for providing them the data points of their paper. AP, OU and MGS acknowledge support from the South African Square Kilometre Array Project as well as from the National Research Foundation.

REFERENCES

Bagla J. S., Khandai N., Datta K. K., 2010, MNRAS, 407, 567
Barnes L. A., Haehnelt M. G., 2010, MNRAS, 403, 870
Barnes L. A., Haehnelt M. G., 2014, MNRAS, 440, 2313
Battye R. A., Browne I. W. A., Dickinson C., Heron G., Maffei B., Pourtsidou A., 2013, MNRAS, 434, 1239
Bernardeau F., Colombi S., Gaztañaga E., Scoccimarro R., 2002, Phys. Rep., 367, 1

Bull P., Ferreira P. G., Patel P., Santos M. G., 2015, ApJ, 803, 21
Bullock J. S., Kolatt T. S., Sigad Y., Somerville R. S., Kravtsov A. V., Klypin A. A., Primack J. R., Dekel A., 2001, MNRAS, 321, 559
Cen R., 2012, ApJ, 748, 121
Chang T.-C., Pen U.-L., Bandura K., Peterson J. B., 2010, Nature, 466, 463
Cooray A., Sheth R., 2002, Phys. Rep., 372, 1
Crighton N. H. M. et al., 2015, MNRAS, 452, 217
Davé R., Katz N., Oppenheimer B. D., Kollmeier J. A., Weinberg D. H., 2013, MNRAS, 434, 2645
Eisenstein D. J., Hu W., 1998, ApJ, 496, 605
Font-Ribera A. et al., 2012, J. Cosmol. Astropart. Phys., 11, 059
Kaiser N., 1987, MNRAS, 227, 1
Kim H.-S., Wyithe J. S. B., Baugh C. M., Lagos C. d. P., Power C., Park J., 2017, MNRAS, 465, 111
Lanzetta K. M., Wolfe A. M., Turnshek D. A., 1995, ApJ, 440, 435
Linder E. V., 2005, Phys. Rev. D, 72, 043529
Marín F. A., Gnedin N. Y., Seo H.-J., Vallinotto A., 2010, ApJ, 718, 972
Martin A. M., Giovanelli R., Haynes M. P., Guzzo L., 2012, ApJ, 750, 38
Masui K. W. et al., 2013, ApJ, 763, L20
Newburgh L. B. et al., 2014, Proc. SPIE Conf. Ser. Vol. 9145, Ground-based and Airborne Telescopes V. SPIE, Bellingham, p. 91454V
Newburgh L. B. et al., 2016, Proc. SPIE, 9906, 99065X
Padmanabhan H., Kulkarni G., 2017, MNRAS, 470, 340
Padmanabhan H., Refregier A., 2017, MNRAS, 464, 4008
Padmanabhan H., Choudhury T. R., Refregier A., 2016, MNRAS, 458, 781
Padmanabhan H., Refregier A., Amara A., 2017, MNRAS, 469, 2323
Peebles P. J. E., 1980, The Large-Scale Structure of the Universe
Planck Collaboration XVI., 2014, A&A, 571, A16
Pontzen A. et al., 2008, MNRAS, 390, 1349
Rahmati A., Schaye J., 2014, MNRAS, 438, 529
Rauch M. et al., 2008, ApJ, 681, 856
Sánchez-Ramírez R. et al., 2016, MNRAS, 456, 4488
Santos M. et al., 2015, in Proc. Sci., Cosmology from a SKA H I Intensity Mapping Survey. SISSA, Trieste, PoS(AASKA14)019
Sarkar D., Bharadwaj S., Anathpindika S., 2016, MNRAS, 460, 4310
Seehars S., Paranjape A., Witzemann A., Refregier A., Amara A., Akeret J., 2016, J. Cosmol. Astropart. Phys., 3, 001
Sheth R. K., Tormen G., 1999, MNRAS, 308, 119
Switzer E. R. et al., 2013, MNRAS, 434, L46
Umeh O., 2017, J. Cosmol. Asropart. Phys., 6, 005
Umeh O., Maartens R., Santos M., 2016, J. Cosmol. Astropart. Phys., 3, 061
Villaescusa-Navarro F., Viel M., Datta K. K., Choudhury T. R., 2014, J. Cosmol. Astropart. Phys., 9, 50
Villaescusa-Navarro F. et al., 2016, MNRAS, 456, 3553
Villaescusa-Navarro F., Alonso D., Viel M., 2017, MNRAS, 466, 2736
Wolfe A. M., Turnshek D. A., Smith H. E., Cohen R. D., 1986, ApJS, 61, 249
Wolfe A. M., Gawiser E., Prochaska J. X., 2005, ARA&A, 43, 861

APPENDIX A: PERTURBATION THEORY FORMULAS

The necessary kernels are: F_2 the non-linear density kernel, G_2 induced by peculiar velocities at second order and K_R arises from non-linear mode coupling (velocity–velocity and velocity–density, Bernardeau et al. 2002)

$$F_2(\boldsymbol{k}_1,\boldsymbol{k}_2) = \frac{5}{7} + \frac{1}{2}\frac{\boldsymbol{k}_1\cdot\boldsymbol{k}_2}{k_1k_2}\left[\frac{k_1}{k_2}+\frac{k_2}{k_1}\right] + \frac{2}{7}\left[\frac{\boldsymbol{k}_1\cdot\boldsymbol{k}_2}{k_1k_2}\right]^2, \quad \text{(A1)}$$

$$G_2(\boldsymbol{k}_1,\boldsymbol{k}_2) = \frac{3}{7} + \frac{1}{2}\frac{\boldsymbol{k}_1\cdot\boldsymbol{k}_2}{k_1k_2}\left[\frac{k_1}{k_2}+\frac{k_2}{k_1}\right] + \frac{4}{7}\left[\frac{\boldsymbol{k}_1\cdot\boldsymbol{k}_2}{k_1k_2}\right]^2, \quad \text{(A2)}$$

$$K_R(\boldsymbol{k}_1,\boldsymbol{k}_2) = f\,b_1\mu_1^2 + f\,b_1\,\mu_2^2 + \mu_1\mu_2\left[f\,b_1\frac{k_1}{k_2} + f\,b_1\frac{k_2}{k_1}\right] + f^2\left[2\mu_1^2\,\mu_2^2 + \mu_1\mu_2\left(\mu_1^2\frac{k_1}{k_2} + \mu_2^2\frac{k_2}{k_1}\right)\right]. \quad \text{(A3)}$$

The matter and velocity power spectra at third order write

$$P_{\rm m}^{13}(k) = \frac{1}{252}\frac{k^3}{4\pi^2}P_{\rm m}^{11}(k)\int_0^\infty {\rm d}r\; P_{\rm m}^{11}(kr)\left[\frac{12}{r^2} - 158 + 100\,r^2 - 42\,r^4 + \frac{3}{r^3}(r^2-1)^3(7r^2+2)\log\left|\frac{1+r}{1-r}\right|\right], \quad \text{(A4)}$$

$$P_{\theta}^{13}(k) = \frac{1}{84}\frac{k^3}{4\pi^2}P_{\rm m}^{11}(k)\int_0^\infty {\rm d}r\; P_{\rm m}^{11}(kr)\left[\frac{12}{r^2} - 82 + 4\,r^2 - 6\,r^4 + \frac{3}{r^3}(r^2-1)^3(r^2+2)\log\left|\frac{1+r}{1-r}\right|\right]. \quad \text{(A5)}$$

The last component of the $P_{\rm H_I}^{13}(k,\mu)$ is

$$I_R(k,\mu) = \frac{k^3}{(2\pi)^2}\int {\rm d}r\,P^{11}(kr)\times\mu^2 f\left([b_2B_1(r) + b_1B_2(r)] + \mu^2 f^2\left[b_1B_3(r) + B_4 + \mu^2(b_1^2B_5(r) + f\,B_6(r))\right]\right) \quad \text{(A6)}$$

with

$$B_1(r) = \frac{1}{6},$$

$$B_2(r) = \frac{1}{84}\left[-2(9r^4 - 24r^2 + 19) + \frac{9}{r}(r^2-1)\log\left(\frac{1+r}{|1-r|}\right)\right],$$

$$B_3(r) = -\frac{1}{3},$$

$$B_4(r) = -\frac{1}{336\,r^3}\left[2(-9\,r^7 + 33\,r^5 + 33\,r^3 - 9\,r) + 9(r^2-1)\log\left(\frac{1+r}{|1-r|}\right)\right],$$

$$B_5(r) = \frac{1}{336\,r^3}\left[2\,r(-27\,r^6 + 63\,r^4 - 109\,r^2 + 9) + 9(3\,r^2+1)(r^2-1)\log\left(\frac{1+r}{|1-r|}\right)\right].$$

Lastly, in this framework, the full one-loop matter power spectrum in real space is

$$P_{\rm m}^{\rm NL}(k) = P_{\rm m}^{11}(k) + P_{\rm m}^{22}(k) + P_{\rm m}^{13}(k), \quad \text{(A7)}$$

where the second-order term writes

$$P_{\rm m}^{22}(k) = \frac{1}{2}\int\frac{{\rm d}^3k_1}{(2\pi)^3}F_2^2(\boldsymbol{k}_1,\boldsymbol{k}_2)P_{\rm m}^{11}(k_2)\,P_{\rm m}^{11}(k_1). \quad \text{(A8)}$$

In redshift space, the full one-loop matter power spectrum is

$$P_{\rm m}^{\rm NL}(k,\mu) = P_{\rm m}^{11}(k,\mu) + P_{\rm m}^{22}(k,\mu) + P_{\rm m}^{13}(k,\mu), \quad \text{(A9)}$$

$$P_{\rm m}^{11}(k,\mu) = \left[1 + f\,\mu^2\right]^2\,P_{\rm m}^{11}(k), \quad \text{(A10)}$$

$$P_{\rm m}^{22}(k,\mu) = \frac{1}{2}\int\frac{{\rm d}^3k_1}{(2\pi)^3}\left[F_2(\boldsymbol{k}_1,\boldsymbol{k}_2) + \mu^2G_2(\boldsymbol{k}_1,\boldsymbol{k}_2) + K_R(\boldsymbol{k}_1,\boldsymbol{k}_2)\right]^2 \times P_{\rm m}^{11}(k_2)\,P_{\rm m}^{11}(k_1), \quad \text{(A11)}$$

$$P_{\rm m}^{13}(k,\mu) = \left(1+\mu^2 f\right)\left\{I_R(k,\mu)\,P_{\rm m}^{11}(k) + \left[P_{\rm m}^{13}(k) + \mu^2\,f\,P_{\theta}^{13}(k)\right]\right\}. \quad \text{(A12)}$$

This paper has been typeset from a TEX/LATEX file prepared by the author.